Heterometallic {Fe<inf>18</inf>M<inf>6</inf>} (M = Y, Gd, Dy) Pivalate Wheels Display Solvent-Induced Polymorphism

CRYSTAL GROWTH & DESIGN

pubs.acs.org/crystal

Article

Heterometallic $\{Fe_{18}M_6\}$ (M = Y, Gd, Dy) Pivalate Wheels Display Solvent-Induced Polymorphism

Published as part of a Crystal Growth and Design virtual special issue on Molecular Magnets and Switchable Magnetic Materials

Daniel Podgornii, Francoise M. Amombo Noa, Jan van Leusen, Christine J. McKenzie, Lars Öhrström,* Paul Kögerler, and Svetlana G. Baca*

Cite This: *Cryst. Growth Des.* 2022, 22, 5526−5534

Read Online

ACCESS | Metrics & More | Article Recommendations | Supporting Information

ABSTRACT: A new series of heterometallic wheels, isolated as $[Fe_{18}M_6(piv)_{12}(Htea)_{18}(tea)_6(N_3)_6]\cdot n(solvent)$ (M^{III} = Y (**1a**, **1b**), Gd (**2a**, **2b**), and Dy (**3a**, **3b**); Hpiv = pivalic acid, H_3tea = triethanolamine), forms by the reaction of trinuclear μ_3-oxo-linked or hexanuclear μ-OH-linked Fe(III) pivalate clusters with rare earth nitrates, H_3tea, and azide ligands in MeOH/MeCN or EtOH/MeCN media under ultrasonic irradiation. Single-crystal X-ray diffraction showed that wheels **1a**−**3a** prepared from MeOH/MeCN solutions crystallize in the triclinic space group $P\bar{1}$ and have C_i symmetry, whereas wheels **1b**−**3b** received from EtOH/MeCN solution crystallize in the trigonal space group $R\bar{3}$ and have C_{3i} symmetry. Magnetic studies reveal medium antiferromagnetic exchange interactions within the Fe_3 trimeric unit (with the exchange coupling parameters of J_{Fe3} = −13.1 cm^{-1} for **1a**, J_{Fe3} = −11.6 cm^{-1} for **1b**) and weak intermolecular antiferromagnetic exchange interactions (λ_{mf} = −0.366 mol cm^{-3} and −0.368 mol cm^{-3} (zJ_{mf} = −0.19 cm^{-1}), respectively). This leads to spin ground states of S = 5/2 for each $\{Fe_3\}$ unit. Substitution of diamagnetic Y(III) centers by paramagnetic Ln(III) centers (in **2a**/**2b** by Gd(III) and in **3a**/**3b** by Dy(III) centers) results in ferromagnetic exchange interactions between the Fe(III) and Ln(III) centers in addition to the predominant antiferromagnetic Fe···Fe interactions in **1a**/**1b**.

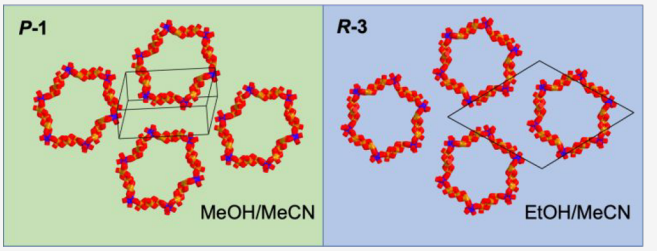

INTRODUCTION

Wheel-shaped polynuclear cluster 3d/4f metals have attracted considerable interest in recent years. Such macrocyclic aggregates, with extensive spherical cavities, can perform the function of supramolecular hosts for binding specific guest molecules, leading to further possible applications in sensing, molecular recognition, host−guest chemistry, catalysis, drug delivery, or gas storage systems.[1] From a magnetic point of view, 3d/4f wheel clusters can also be regarded as approximations for infinite chains and—depending on their symmetry—can exhibit unusual magnetic properties including single-molecule magnet (SMM) behavior, exotic spin frustration effects, metamagnetic phase transitions, and others.[2,3] Thus, the specific architecture, fascinating physical properties, and the potential in a variety of applications ranging from nanoscale magnetic materials to catalysts motivate the development of new and improved synthetic routes to wheel-shaped clusters. To date, much previous research has focused on the design and investigation of pure transition-metal-based wheel-like systems, mostly aiming at the construction of functional materials possessing SMM properties. Among them are the ultralarge $\{Mn_{84}\}$ "SMM manganese wheel" prepared by Christou et al.,[4] optically active paramagnetic $\{Fe_{28}\}$ "ferric wheels" reported by Clérac and co-workers,[5] calixarene-supported $\{Co_{24}\}$ designed by Gao et al.,[6] the first "nickel wheel" SMM based on a cyclic $\{Ni_{12}\}$ complex showing resonant quantum tunnelling of magnetization[7] and $\{Cr_7Ni\}$ heterometallic rings using qubits[8] constructed by Winpenny's group, and Christou's $\{Ga_{20}\}$ "gallic wheel".[9] Later on, the exploration of the effects of incorporating f-element ions, usually carrying highly anisotropic magnetic moments,[10−13] into 3d metal-based wheel architectures[14−16] became a significant trend in preparative coordination chemistry, exemplified by Gao's octanuclear $\{Mn^{III}_4Ln^{III}_4\}$ (Ln = Sm, Tb, Dy) formate wheels[17] and Tang's dodecanuclear $\{Co^{II}_2Dy^{III}_{10}\}$ acetate wheel[18] showing SMM behavior. Powell et al. designed a family of rare oxygen-bridged 20-nuclear $\{Fe^{III}_{16}Ln^{III}_4\}$ (Ln = Sm, Eu, Gd, Dy, Tb, Ho) acetate wheels.[19] Unprecedented 40-nuclear $\{Co^{II}_{16}Ln^{III}_{24}\}$ and 60-nuclear $\{Cu^{II}_{36}Ln^{III}_{24}\}$ (Ln = Dy and Gd)

Received: June 3, 2022
Revised: August 9, 2022
Published: August 23, 2022

https://doi.org/10.1021/acs.cgd.2c00620
Cryst. Growth Des. 2022, 22, 5526−5534

wheels where the gadolinium derivative exhibited a relatively large magnetocaloric effect were obtained by Tong et al.[20,21]

In a previous study[22] we presented a new synthetic procedure for ultralarge 3d/4f isobutyrate-based wheels of the type $\{Fe^{III}_{18}M^{III}_{6}\}$ (M = Dy, Gd, Tb, Ho, Sm, Eu, and Y) using ultrasonication of MeOH/MeCN or MeOH/EtOH solutions of μ_3-oxo-bridged trinuclear Fe^{III} isobutyrate clusters, lanthanide/yttrium nitrates, and bridging triethanolamine (H_3tea) and azide ligands. Since carboxylato bridging ligands (R−COO) have the potential to determine the curvature of the resulting wheel segments due to the steric requirements of their organic groups, we explored the possibility of replacing isobutyrate (R = *iso*-propyl). Herein, we extend this approach to pivalates, R = *tert*-butyl, expected to show a higher steric demand. This has mandated the use different iron complex precursors for the introduction of the respective carboxylate. To this effect, we show how to employ both trinuclear μ_3-oxo-bridged and hexanuclear μ-OH-bridged Fe^{III} pivalate clusters ($[Fe_3O(piv)_6(H_2O)_3]$piv·2(Hpiv) or $[Fe_6(OH)_2(piv)_{12}]$) under otherwise similar synthetic conditions. Using these precursors, a series of wheel compounds $[Fe_{18}M_6(piv)_{12}(Htea)_{18}(tea)_6(N_3)_6]\cdot n$(solvent) (where M^{III} = Y (**1a**, **1b**), Gd (**2a**, **2b**), and Dy (**3a**, **3b**)) has been isolated. Variation of media (e.g., MeOH/MeCN vs EtOH/MeCN) results in the formation of two polymorphic modifications ($P\bar{1}$ for **1a**−**3a** vs $R\bar{3}$ for **1b**−**3b**), in which different interwheel hydrogen-bonded supramolecular networks of a 4-connected **sql** or a 6-connected **pcu** topologies, respectively, can be observed. Additionally, the resulting supramolecular structures show infinite channels: $P\bar{1}$ polymorphs have the more hydrophilic nature of the formed channels compared to the hydrophobic character of the channels in the $R\bar{3}$ polymorphs. The title compounds were characterized by elemental analysis, IR spectroscopy, electrospray-ionization mass spectrometry, thermogravimetric analysis, X-ray diffraction, and magnetic studies. Their magnetic properties (dc and ac measurements) are discussed, and a correlation with their respective structural features is made.

EXPERIMENTAL SECTIOM

Materials and Physical Measurements. All manipulations were performed under aerobic conditions using chemicals and solvents as received without further purification. μ_3-Oxo trinuclear $[Fe_3O(piv)_6(H_2O)_3]$piv·2(Hpiv) and μ_3-OH hexanuclear $[Fe_6(OH)_2(piv)_{12}]$ pivalate clusters have been prepared as published.[23,24] ***Caution!****Care should be taken when using potentially explosive metal azide compounds.* IR spectra were recorded on a PerkinElmer Spectrum Series 815 FT-IR spectrometer in the 600−4000 cm^{-1} region. TGA measurements were carried out with a Mettler Toledo TGA/DSC 3+ 851 in air at a heating rate of 10 K min^{-1} from 30 to 800 °C. Electrospray-ionization mass spectrometry (ESI-MS) was performed on a ThermoFisher Scientific LTQ-Orbitrap XL mass spectrometer in positive ion detection mode; the samples were prepared by dissolving the title compounds in methanol or tetrahydrofuran containing 0.1% acetic acid. An Elmasonic P ultrasonic bath operating at 37 kHz was used for ultrasonic irradiation.

Syntheses. *Synthesis of* ***1a*** *{$Fe_{18}Y_6$-MeOH}.* To the solution of $[Fe_3O(piv)_6(H_2O)_3]$piv·2(Hpiv) (0.115 g, 0.1 mmol), $Y(NO_3)_3\cdot 6H_2O$ (0.069 g, 0.18 mmol), and sodium azide (0.020 g, 0.31 mmol) in MeCN (6 mL) was added a solution of triethanolamine (0.370 g, 2.5 mmol) in MeOH (6 mL). The resulting solution was treated under ultrasonic irradiation for 30 min and then filtered. The filtrate was left for slow evaporation of the mother solution at room temperature. This gave yellow crystals suitable for X-ray analysis of **1a** after 2 to 3 weeks. The crystals were filtered off, washed with MeCN, and dried in the air. Yield: 0.055 g, 48% (based on Fe). The crystals of **1a** lost crystallinity rapidly after filtering due to the loss of some solvent molecules. Elemental analysis calcd. for **1a** $[Fe_{18}Y_6(piv)_{12}(Htea)_{18}(tea)_6(N_3)_6]\cdot 20H_2O$: C, 35.56; H, 6.64; N, 8.54%. Found: C, 35.55; H, 6.33; N, 8.13%. IR (cm^{-1}): 3386 (br), 2955 (sh), 2902 (sh), 2856 (m), 2064 (s), 1584 (sh), 1562 (m), 1527 (m), 1481 (m), 1458 (m), 1426 (sh), 1411 (s), 1356 (m), 1305 (sh), 1256 (w), 1223 (m), 1163 (w), 1096 (sh), 1071 (vs), 1032(sh), 1000 (sh), 916 (sh), 895 (s), 809 (sh), 791 (m), 749 (m).

1b *{$Fe_{18}Y_6$-EtOH}.* To the solution of $[Fe_3O(piv)_6(H_2O)_3]$piv·2(Hpiv) (0.115 g, 0.1 mmol), $Y(NO_3)_3\cdot 6H_2O$ (0.069 g, 0.18 mmol), and sodium azide (0.020 g, 0.31 mmol) in MeCN (6 mL) was added a solution of triethanolamine (0.370 g, 2.5 mmol) in EtOH (6 mL). The resulting solution was treated under ultrasonic irradiation for 30 min and filtered afterward. The filtered mixture was left for slow evaporation of the mother solution. This gave crystals of **1b**. Yield: 0.05 g, 43% (based on Fe). The crystals of **1b** rapidly lost crystallinity after filtering due to the loss of some solvent molecules. Elemental analysis calcd. for **1b** $[Fe_{18}Y_6(piv)_{12}(Htea)_{18}(tea)_6(N_3)_6]\cdot 20H_2O$: C, 35.56; H, 6.64; N, 8.54%. Found: C 35.61; H, 6.20; N, 8.25%. IR (cm^{-1}): 3398 (br), 2958 (sh), 2898 (sh), 2856 (m), 2068 (s), 1586 (sh), 1564 (m), 1528 (m), 1482 (m), 1460 (m), 1429 (sh), 1411 (s), 1357 (m), 1305 (sh), 1257 (w), 1223 (m), 1164 (w), 1094 (sh), 1072 (vs), 1032 (sh), 1000 (sh), 916 (sh), 896 (s), 809 (sh), 791 (m), 749 (m). Complexes **2** and **3** have been obtained in an analogous manner to **1** except that $Gd(NO_3)_3\cdot 6H_2O$ and $Dy(NO_3)_3\cdot 6H_2O$ were used as a resource of Ln(III) ions.

2a *{$Fe_{18}Gd_6$-MeOH}.* Yield: 0.081 g, 66% (based on Fe). The crystals of **2a** lost crystallinity rapidly after filtering due to the loss of some solvent molecules. Elemental analysis calcd. for **2a** $[Fe_{18}Gd_6(piv)_{12}(Htea)_{18}(tea)_6(N_3)_6]\cdot 20H_2O$: C, 33.56; H, 6.27; N, 8.06%. Found: C, 33.52; H, 6.15; N, 7.74%. IR (cm^{-1}): 3386 (br), 2955 (sh), 2902 (sh), 2856 (m), 2064 (s), 1584 (sh), 1562 (m), 1527 (m), 1481 (m), 1458 (m), 1426 (sh), 1411 (s), 1356 (m), 1305 (sh), 1256 (w), 1223 (m), 1163 (w), 1096 (sh), 1071 (vs), 1032 (sh), 1000 (sh), 916 (sh), 895 (s), 809 (sh), 791 (m), 749 (m).

2b *{$Fe_{18}Gd_6$-EtOH}.* Yield: 0.055 g, 45% (based on Fe). The crystals of **2b** lost crystallinity rapidly after filtering due to the loss of some solvent molecules. Elemental analysis calcd. for **2b** $([Fe_{18}Gd_6(piv)_{12}(Htea)_{18}(tea)_6(N_3)_6]\cdot 20H_2O$: C, 33.56; H, 6.27; N, 8.06%. Found: C, 33.50; H, 5.91; N, 7.73%. IR (cm^{-1}): 3395 (br), 2957 (sh), 2895 (sh), 2857 (m), 2064 (s), 1584 (sh), 1562 (m), 1526 (m), 1481 (m), 1459 (m), 1411 (s), 1356 (m), 1305 (sh), 1258 (w), 1223 (m), 1161 (w), 1096 (sh), 1070 (vs), 1033 (sh), 1000 (sh), 894 (s), 809 (sh), 790 (m), 749 (m).

3a *{$Fe_{18}Dy_6$-MeOH}. Method A.* Complex **3a** was obtained in an analogous manner to **1** except that $Dy(NO_3)_3\cdot 6H_2O$ was used as a resource of Ln(III) ions.Yield: 0.058 g, 48% (based on Fe). The crystals of **3a** lost crystallinity rapidly after filtering due to the loss of some solvent molecules. Elemental analysis calcd. for **3a** $([Fe_{18}Dy_6(piv)_{12}(Htea)_{18}(tea)_6(N_3)_6]\cdot 21H_2O$: C, 33.33; H, 6.25; N, 8.00%. Found: C, 33.30; H, 6.01; N, 7.63%. IR (cm^{-1}): 3388 (br), 2955 (sh), 2901 (sh), 2857 (m), 2060 (s), 1584 (sh), 1563 (m), 1528 (m), 1481 (m), 1456 (m), 1426 (sh), 1410 (s), 1356 (m), 1307 (sh), 1256 (w), 1223 (m), 1163 (w), 1096 (sh), 1071 (vs), 1021(sh), 998 (sh), 916 (sh), 895 (s), 807 (sh), 791 (m), 749 (m).

Method B. A hexanuclear $[Fe_6(OH)_2(piv)_{12}]$ (115 mg, 0.071 mmol) cluster was used in a similar reaction as the source of Fe(III) ions. Yield: 0.031 g, 27% (based on Fe).

3b *{$Fe_{18}Dy_6$-EtOH}.* Yield: 0.062 g, 51% (based on Fe). The crystals of **3b** lost crystallinity rapidly after filtering due to the loss of some solvent molecules. Elemental analysis calcd. (%) for **1b** $[Fe_{18}Dy_6(piv)_{12}(Htea)_{18}(tea)_6(N_3)_6]\cdot 20H_2O$: C, 33.42; H, 6.24; N, 8.02%. Found: C, 33.53; H, 6.08; N, 7.80%. IR (cm^{-1}): 3386 (br), 2955 (sh), 2902 (sh), 2856 (m), 2064 (s), 1584 (sh), 1562 (m), 1527 (m), 1481 (m), 1458 (m), 1426 (sh), 1411 (s), 1356 (m), 1305 (sh), 1256 (w), 1223 (m), 1163 (w), 1096 (sh), 1071 (vs), 1032 (sh), 1000 (sh), 916 (sh), 895 (s), 809 (sh), 791 (m), 749 (m).

X-ray Crystallographic Analyses. Suitable crystals with an appropriate size and having the ability to extinguish plane-polarized light were mounted onto the tip of a loop using Paratone N oil. The mounted crystal was then placed on a goniometer head attached to a

https://doi.org/10.1021/acs.cgd.2c00620
Cryst. Growth Des. 2022, 22, 5526−5534

diffractometer. **1a** and **2a** X-ray intensity data were recorded on a Bruker D8 venture diffractometer. The venture instrument is equipped with both Cu (λ = 1.54184 Å) and Mo (λ = 0.71073 Å) microfocus X-ray sources and a Photon III CPAD detector. Data reduction was conducted using SAINT-Plus software,[25] while the absorption corrections were performed using the SADABS program.[26,27] For **1b**, **2b**, and **3b**, single crystal X-ray diffraction data were collected on a Rigaku XtaLAB Synergy-S Dualflex diffractometer equipped with an AtlasS2 detector using Cu Kα radiation (λ = 1.54184 Å). The XtaLAB synergy-S is equipped with a HyPix-6000 HE detector using Mo Kα radiation (λ = 0.71073 Å); diffraction data were acquired and processed with the CrysAlisPro software package.[28,29] For **3a**, all measurements were made on an Oxford Diffraction SuperNova area-detector diffractometer using mirror optics monochromated Mo Kα radiation (λ = 0.71073 Å). Crystal structures for **1a**, **2a**, and **1b**−**3b** were collected at 100 K and for **3a** at 123 K, and direct methods were used for all structures. The refinements were established by full-matrix least-squares with SHELX-2018/3[30] using X-seed software.[31] CrystalMaker was used for all structure drawings.[32] All solvent molecules in the structural cavities were squeezed using Platon software[33] due to excessive disorder. Non-hydrogen atoms were refined anisotropically except in the case of disorder. Hydrogen atoms were placed in calculated positions. The crystallographic data and structure refinement parameters for **1**−**3** are listed in Table 1, and additional crystallographic information is available in the Supporting Information, Table S1. The selected bond distances for **1**−**3** are given in Table S2.

Magnetic Measurements. Magnetic susceptibility data of **1**−**3** were recorded using a Quantum Design MPMS-5XL SQUID magnetometer for direct current (dc) and alternating current (ac) measurements. The polycrystalline samples were immobilized into polytetrafluoroethylene (PTFE) capsules. The dc susceptibility data were acquired as a function of the field (0.1−5.0 T) and temperature (2.0−290.0 K). The ac susceptibility data were measured at zero or 500 Oe static bias field in the frequency range 3−1500 Hz (T = 2.0−50.0 K, B_{ac} = 3 G). However, no relevant (**2a**, **2b**) out-of-phase signals or no signals analyzable in terms of a general Debye expression (**3a**, **3b**) could be detected. The data were corrected for diamagnetic contributions from the sample holder and the compounds ($\chi_{m,dia}/10^{-3}$ cm^3 mol^{-1} = −3.29 (**1a**), −3.27 (**1b**), −3.52 (**2a**), −3.47 (**2b**), −3.47 (**3a**), −3.53 (**3b**)).

RESULTS AND DISCUSSION

In the synthesis of high-nuclearity carboxylate clusters, the heating of μ_3-oxo trinuclear homo- and heterometallic coordination clusters with polyfunctional ligands in the solid state or in high-boiling solvents, as well as under solvothermal and microwave treatment, has been especially successful.[34−36] The use of ultrasonication for the chemical synthesis of nanoarchitectures has recently emerged as a promising tool.[37] Such a methodology of using ultrasonic irradiation for syntheses can affect the reaction rates, purity, and yields in comparison to conventional heating and is a simple, rapid, and economic green method. In this regard, the application of a sonochemical approach in the fabrication of different types of heterometallic Fe/Ln clusters under mild conditions[22,35,38] offers significant potential. Recently, the hexanuclear Mn^{II}/Mn^{III} isobutyrate cluster was exposed to ultrasonication that led to the assembly of the biggest known heterometallic Mn−Dy oxo-hydroxo-isobutyrate cluster, $[Mn_{26}Dy_6O_{16}(OH)_{12}(ib)_{42}]$, showing SMM properties.[39] Ultrasonication of a mixture MeOH/MeCN or EtOH/MeCN (1:1) containing μ_3-oxo trinuclear pivalate clusters $[Fe_3O(piv)_6(H_2O)_3]piv{\cdot}2(Hpiv)$, $M(NO_3)_3{\cdot}6H_2O$ (M^{III} = Y, Gd, and Dy) salts, and sodium azide and triethanolamine (H_3tea) ligands gave tetraicosanuclear $\{Fe^{III}{}_{18}M^{III}{}_6\}$-type $[Fe_{18}M_6(piv)_{12}(Htea)_{18}(tea)_6(N_3)_6]{\cdot}n$(solvent) (where M = Y (**1a**, **1b**), Gd (**2a**, **2b**), and Dy (**3a**, **3b**) pivalate wheel-shaped clusters in good yields. Cluster **3a** can also

Table 1. Crystallographic Data and Structure Refinement Parameters for 1−3

	1a	1b	2a	2b	3a	3b
formula[a]	$C_{204}H_{414}Fe_{18}N_{42}O_{96}Y_6$	$C_{204}H_{414}Fe_{18}N_{42}O_{96}Y_6$	$C_{204}H_{414}Fe_{18}Gd_6N_{42}O_{96}$	$C_{204}H_{414}Fe_{18}Gd_6N_{42}O_{96}$	$C_{204}H_{414}Dy_6Fe_{18}N_{42}O_{96}$	$C_{204}H_{414}Fe_{18}Dy_6N_{42}O_{96}$
data collection temp. (K)	100(2)	100(2)	100(2)	100(2)	123(2)	100(2)
crystal system	triclinic	trigonal	triclinic	trigonal	triclinic	trigonal
space group	$P\bar{1}$	$R\bar{3}$	$P\bar{1}$	$R\bar{3}$	$P\bar{1}$	$R\bar{3}$
a (Å)	16.6880(7)	34.2943(16)	16.5731(7)	32.9580(10)	15.0102(10)	33.2372(12)
b (Å)	21.3119(10)	34.2943(16)	21.2776(9)	32.9580(10)	20.5135(10)	33.2372(12)
c (Å)	27.2034(10)	30.0089(10)	27.3103(12)	30.1746(6)	28.9137(16)	30.2698(10)
α (deg)	97.287(3)	90	97.909(2)	90	107.005(5)	90
β (deg)	93.391(2)	90	93.309(2)	90	90.138(5)	90
γ (deg)	111.460(3)	120	111.118(2)	120	103.537(5)	120
V (Å^3)	8872.9(7)	30565(3)	8838.1(7)	28385.3(18)	8253.0(9)	28959(2)
Z	1	3	1	3	1	3
final R indices [$I > 2\sigma(I)$]	R_1 = 0.0844	R_1 = 0.1101	R_1 = 0.0596	R_1 = 0.1058	R_1 = 0.0949	R_1 = 0.0958
	wR_2 = 0.2305	wR_2 = 0.3264	wR_2 = 0.1638	wR_2 = 0.3200	wR_2 = 0.2128	wR_2 = 0.2645
R indices (all data)	R_1 = 0.1226	R_1 = 0.1486	R_1 = 0.0747	R_1 = 0.1222	R_1 = 0.1799	R_1 = 0.1280
	wR_2 = 0.2571	wR_2 = 0.3601	wR_2 = 0.1731	wR_2 = 0.3382	wR_2 = 0.2527	wR_2 = 0.2857
CCDC no.	2169642	2169643	2169644	2169645	2169646	2169647

[a]Molecular formulas of **1**−**3** correspond here to the structures after SQUEEZE procedure.

https://doi.org/10.1021/acs.cgd.2c00620
Cryst. Growth Des. 2022, 22, 5526−5534

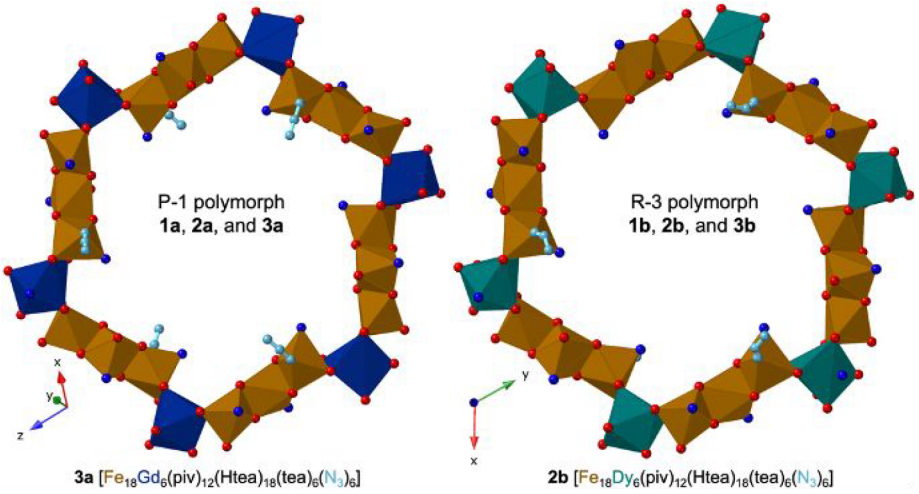

Figure 1. Comparison of the overall molecular wheel structure of the $P\bar{1}$ and $R\bar{3}$ polymorphs of $[Fe_{18}M_6(piv)_{12}(Htea)_{18}(tea)_6(N_3)_6]$. Specifically, **2a** ($P\bar{1}$ $\{Fe_{18}Gd_6\}$) and Dy analogue **3b** ($R\bar{3}$ $\{Fe_{18}Dy_6\}$) have been drawn in this figure, but their analogues are similar.

be prepared from hexanuclear $[Fe_6(OH)_2(piv)_{12}]$ clusters in MeOH/MeCN media. The TGA experiments were performed to determine the thermal stability of $\{Fe_{18}Ln/Y_6\}$ pivalate wheels (Figures S2−S7). Wheels **1**−**3** were further characterized by IR and ESI-MS.

The IR spectra of **1**−**3** display a very strong peak in the range of 2061−2069 cm^{-1} that corresponds to the N≡N stretching vibrations of azide ligands in all compounds. In addition, there are very strong bands in the 1563−1528 cm^{-1} and 1410−1406 cm^{-1} regions that arise from the asymmetric and symmetric vibrations of the carboxylate groups from the coordinated pivalates, respectively. The C−H asymmetric and symmetric stretching vibrations for methyl groups of carboxylates are observed in the range of 2959−2870 cm^{-1}, while the asymmetric and symmetric bending vibrations for these groups produce a strong single band in the region 1481 cm^{-1} and a doublet in the region 1374−1355 cm^{-1}, respectively. The presence of the uncoordinated hydroxyl groups of $Htea^{2-}$ and solvent molecules caused the appearance of broad absorption bands in the region of 3420−3375 cm^{-1}.

ESI-MS was used to deduce information on the fragmentation characteristics of **1**−**3** under gas phase ionization conditions. Mass spectra of **1**−**3** showed several different fragmentation pathways, depending on the Ln/Y ions. A summary of the fragments detected in the ESI mass spectra of **1**−**3** in MeOH or thf is given in Table S3. A difference between neighboring peaks in the fragment series of **1**−**3** equals m/z = 202 (Δ), which can be identified as the loss of one negatively charged tea^{3-} moiety and one Fe^{3+} cation from the corresponding fragment. In ESI-MS of **1a** and **1b** recorded in positive mode, the peaks of 100% relative intensity are attributed to pentanuclear $[Fe_4Y(piv)(tea)_4(MeO)]^+$ (m/z 1029) and trinuclear $[Fe_2Y(tea)_2(Htea)]^+$ (m/z 640) fragment ions in MeOH or thf, respectively. The formation of these different polynuclear heterometallic fragments was clearly identified as the isotope patterns are consistent with their assignment (see Figure S1). Further, ESI-MS **1a** and **1b** in MeOH solution show similar fragmentation patterns, and the corresponding peaks result from the loss of a tea^{3-} residue and an Fe cation in the fragments with a general formula of $[Fe_{3-x}Y(tea)_{3-x}(Htea)]^+$ (x = 0, 1; m/z 842, 640). The next series reveal polynuclear fragments as well as solvated species: $[Fe_{6-x}Y(piv)(tea)_{6-x}(MeO)]^+$ (x = 0−3, m/z = 1433, 1231, 1029, and 827); $[Fe_{5-x}Y(piv)_2(tea)_{5-x}]^+$ (x = 0−2, m/z = 1301, 1099, and 897); $[Fe_{6-x}Y(piv)_2(tea)_{4-x}(Htea)_3]^+$ (x = 0−3, m/z = 1652, 1450, 1248, and 1046); $[Fe_{5-x}Y_2(piv)_2(tea)_{6-x}]^+$ (x = 0−2, m/z = 1536, 1334, and 1077); $[Fe_{6-x}Y_2(tea)_{7-x}(Htea)(H_2O)_4]^+$ (x = 0, 1; m/z = 1755, 1553). The spectra for **1a**/**1b** recorded in thf contain only signals corresponding to $[Fe_{6-x}Y(tea)_{6-x}(Htea)]^+$ (x = 0−4) and $[Fe_{5-x}Y(tea)_{3-x}(Htea)_2(N_3)_4(H_2O)_2]^+$ (x = 0, 1; m/z = 1103, 1305) fragments. For the ESI-MS$^+$ of **2a** in MeOH, almost similar fragmentation pathways are observed with the base peak corresponding to pentanuclear $[Fe_4Gd(piv)(tea)_4(MeO)]^+$ species at m/z 1098 (see Table S3 and Figure S1c). The difference comes from the presence of a cationic $\{[Fe_4Gd_2(tea)_6(H_2O)_8]+H\}^+$ fragment (m/z 1561, 77%), which in the MS of **2a** recorded in thf exhibits 100% relative intensity. The patterns for **3a** (in MeOH or thf solution) contain peaks of 100% intensity for trinuclear $[Fe_2Dy(tea)_2(Htea)]^+$ (m/z 715) fragments, whereas **3b** exhibits a 100% peak at m/z 1570 corresponding to the heptanuclear $[Fe_5Dy_2(piv)_2(tea)_4(OH)_3(MeO)_3(MeOH)]^+$ fragment.

X-ray Crystal Structures. Single crystal X-ray diffraction analyses revealed that compounds **1a**, **2a**, and **3a** prepared from MeOH/MeCN solution crystallize in the triclinic space group $P\bar{1}$ and have C_i symmetry, whereas wheels **1b**, **2b**, and **3b**, received from EtOH/MeCN media, crystallize in the trigonal space group $R\bar{3}$ and have C_{3i} crystallographic symmetry (Table 1). Similar to previously reported $\{Fe_{18}M_6\}$ isobutyrate compounds,[22] the core structures of **1**−**3** have a wheel-shaped arrangement of 18 Fe^{III} and six Ln^{III}/Y^{III} ions interconnected by 12 pivalates and 24 triethanolamine ligands, thus the effect on the curvature due to the increased steric demands of the extra methyl group are negligible and will not change the wheel size (i.e., across the wheel, the Dy···Dy distance in the two analogs has increased only 2% for **3b** compared to the previous compound). All iron atoms in **1**−**3** are found in the formal oxidation state +3 (BVS: 2.84−3.12, Table S4). The iron oxidation state assignment is consistent with an analysis of Fe^{II} and Fe^{III} structures from the Cambridge Structural Database (Figure S8). For example, in **2b**, all Fe−O bonds are shorter than 2.05 Å as are the large majority of observed Fe^{III}−O bonds, whereas the majority of Fe^{II}−O bonds are longer than 2.05 Å. The monodentate azide ligands completed the coordination

https://doi.org/10.1021/acs.cgd.2c00620
Cryst. Growth Des. 2022, 22, 5526−5534

spheres of six Fe atoms. In the wheel core, three Fe^{III} ions alternate with one Ln^{III}/Y^{III} ion to form $\{Fe_3Ln/Y\}$ fragments, thus the wheels are slightly puckered, with the Fe···Fe···Fe angles being 128−137° and Fe···Ln/Y···Fe angles being 111−114°. Nearest-neighbor Fe···Fe distances vary from 3.147(3) to 3.228(3) Å and Ln/Y···Fe distances from 3.368(1) to 3.550(1) Å, see Figure 1.

The Fe atoms in the wheels are six-coordinated in an irregular octahedral geometry but with different coordination environments (NO_5 or N_2O_4), and all Ln/Y sites are eight-coordinated (distorted square antiprismatic NO_7 geometry, with a substantially longer Ln/Y−N distance of around 2.6 Å versus the Ln/Y−O of around 2.3 Å, see Figure S8). One pivalate bridges Fe and Ln/Y; the other is attached as monodentate to Ln/Y with a nonbonded Ln/Y···O distance of around 3.8 Å but hydrogen bonding to a $Htea^{2-}$ ligand (O···O ca. 2.5 Å). All 12 pivalates point out from the wheel, six in the equatorial direction and six in a more axial direction. Six of the tea^{3-} ligands form the inner perimeter of the wheel with an intact noncoordinated alcohol group hydrogen bonding to a coordinated tea oxygen atom (O···O ca. 2.6 Å) and 18 in more axial positions forming the rim of the wheel. Six of these have intact −OH groups and form intrawheel hydrogen bonds, whereas six more have intact −OH groups that protrude from the wheel and make the interwheel hydrogen bonds.

These interwheel hydrogen bonds are what differ between the polymorphs. In Figure 2, we have drawn space filling models of

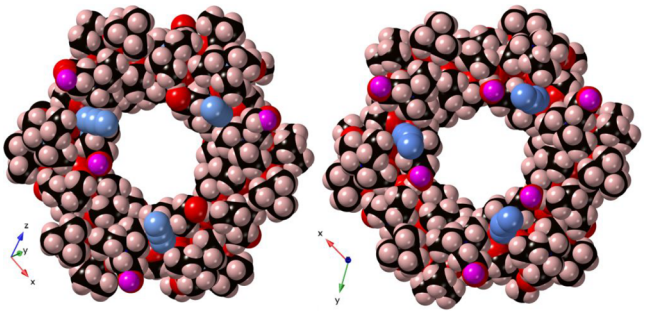

Figure 2. Space filling models of the $P\bar{1}$ and $R\bar{3}$ polymorphs of $[Fe_{18}M_6(piv)_{12}(Htea)_{18}(tea)_6(N_3)_6]$. Specifically, **3a** ($P\bar{1}$ $\{Fe_{18}Gd_6\}$) and **3b** ($R\bar{3}$ $\{Fe_{18}Gd_6\}$) have been drawn in this figure, but their analogues are similar. Pink atoms mark intermolecular hydrogen bond sites (four for $P\bar{1}$ and six for $R\bar{3}$).

1a ($P\bar{1}$ $\{Fe_{18}Y_6\}$) and **3b** ($R\bar{3}$ $\{Fe_{18}Dy_6\}$) with the hydrogen bond sites marked in pink. For **1a** ($P\bar{1}$ $\{Fe_{18}Y_6\}$) only one of the alcohol groups in the inner perimeter forms hydrogen bonds to another wheel, while all three alcohol groups in **2b** ($R\bar{3}$ $\{Fe_{18}Dy_6\}$) form intermolecular hydrogen bonds. On the outer perimeter, all free −OH groups hydrogen bond in both polymorphs. These intermolecular hydrogen bonds have O···O distances on the order of 2.7−3.0 Å. The azide groups appear to have no significant intermolecular interaction and, as is clear from Figure 2, the rest of the surface of the wheels is very hydrophobic.

The hydrogen bonds make for **1a** ($P\bar{1}$ $\{Fe_{18}Y_6\}$) and isostructural analogs a total of eight intermolecular hydrogen bonds forming sheets in the crystallographic *xy* plane. These sheets take the form of a 4-connected **sql**-net by double hydrogen bonds, which makes sense of the close to 90° α and β angles, see Figure 3. The sheets are packed with a slight staggering caused by the 111° γ angle, explaining the long *c* axis.

For the ($R\bar{3}$ $\{Fe_{18}Dy_6\}$) and the related compounds, a total of 12 intermolecular hydrogen bonds form a 3D 6-connected network with the **pcu** topology. The crystallographic *z* axis is aligned with the C_3 axis of the constituent octahedra of the net, giving the 120° of the $R\bar{3}$ space group, and also the *x* and *y* axes line up with the net, see Figure 3.

The wheels have a hole of ca. 1 nm, while the external diameter is ca. 3.4 nm. The crystal structures of wheels display infinite channel formation filled by solvent molecules parallel to the crystal *c* axis for the $R\bar{3}$ polymorphs **1b**, **2b**, and **3b**, and along the *a* axis for the $P\bar{1}$ polymorphs. Upon removal of solvent molecules, the triclinic structures reveal a large total potential solvent area volume of *ca.* 43%, with a sphere fitting in the center of the wheel with a diameter of 9.4 Å, and a trigonal one of *ca.* 48% with a sphere fitting in the center of the wheel with a diameter of 10.7 Å, per unit cell volume, as calculated by CrystalMaker. Solvent loss upon drying rapidly deteriorated the single crystals.

While the hydrogen bonds, as discussed above, may have something to do with the appearance of the two polymorphs, the absence of similar hydrogen bond patterns in the earlier reported analogues $[Fe_{18}Ln_6(O_2CCHMe_2)_{12}(Htea)_{18}(tea)_6(N_3)_6]$, differing by a methyl group in the carboxylate ligand, suggests that there are other factors to consider. In Figure 4, the hydrophobic character of the channels in the $R\bar{3}$ polymorph can be seen, as opposed to the more hydrophilic nature of the unevenly formed channels in the $P\bar{1}$ polymorph. The $R\bar{3}$ polymorph is consistently formed in ethanolic solutions, whereas the $P\bar{1}$ one appears from methanolic solutions, thus one possible driving force may be that ethanol is better suited for the hydrophobic channels. Unfortunately, in neither of these structures is the solvent ordered enough to be determined, so this question remains open.

Wheels **1a**−**3a** are isostructural, as well as the series of **1b**−**3b**, therefore, only a description of Gd analogue **2a** ($P\bar{1}$ $\{Fe_{18}Gd_6\}$) and Dy analogue **3b** ($R\bar{3}$ $\{Fe_{18}Dy_6\}$) will be given here. Figure S8 summarizes the M−O and M−N distances. As can be seen in Figure S8, no significant difference can be found between the two compounds. Fe−azide bond lengths are consistently shorter and the Fe−amine bonds longer. Thermal ellipsoid plots are given in Figure S9.

Magnetic Properties. SQUID measurements were performed on compounds **1a**−**3b** to characterize their magnetic properties. The corresponding data are shown in Figure 5 as $\chi_m T$ vs T plots at 0.1 T and M_m vs B plots at 2.0 K. All compounds including the same Ln(III) centers show very similar behaviors. Both compounds composed of solely Fe(III) centers as paramagnetic species, **1a** and **1b**, reach a $\chi_m T$ value of 45.50 and 48.84 $cm^3\,K\,mol^{-1}$, respectively, at 290 K (Figure 5a). These values are significantly below the range 73.1−81.0 $cm^3\,K\,mol^{-1}$ expected[40] for 18 noninteracting high spin Fe(III) centers. Upon cooling the compounds, the $\chi_m T$ values continuously decrease and drop off below 15 K reaching 14.95 (**1a**) and 14.88 $cm^3\,K\,mol^{-1}$ (**1b**), respectively, at 2.0 K. At this temperature, the molar magnetizations M_m of both compounds show an almost identical dependence on the applied magnetic field B (see Figure 5b). The magnetizations distinctly increase in the range from zero to 1.5 T and slightly increase between 1.5 and 5.0 T. At 5.0 T, M_m is 25.0 $N_A\,\mu_B$ for both compounds, indicating a saturation step well below the expected value for 18 noninteracting Fe(III) centers of 90 $N_A\,\mu_B$.

For a quantified estimation of the magnetism of the Fe(III) constituents, we consider the following approximations. The 18

https://doi.org/10.1021/acs.cgd.2c00620
Cryst. Growth Des. 2022, 22, 5526−5534

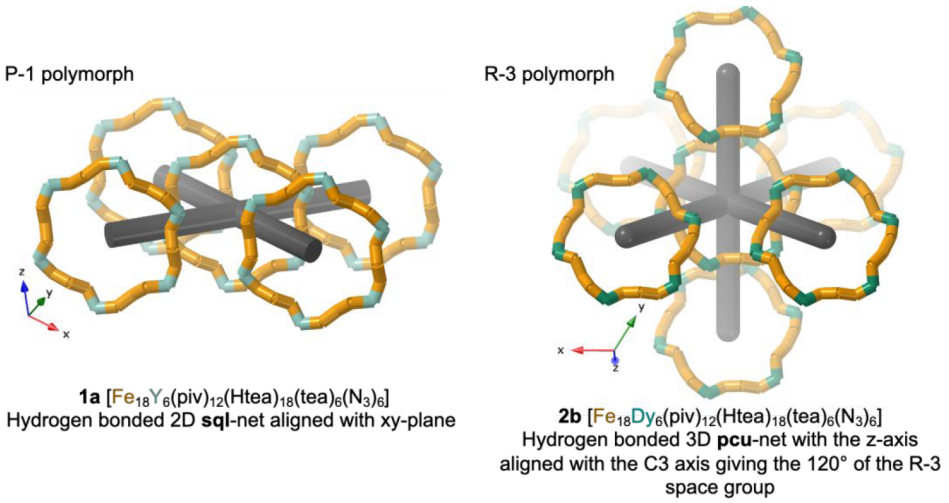

Figure 3. Hydrogen bond networks in the $P\bar{1}$ and $R\bar{3}$ polymorphs of $[Fe_{18}M_6(piv)_{12}(Htea)_{18}(tea)_6(N_3)_6]$. Specifically, **3a** ($P\bar{1}$ $\{Fe_{18}Gd_6\}$) and **3b** ($R\bar{3}$ $\{Fe_{18}Gd_6\}$) have been drawn in this figure, but their analogues are similar.

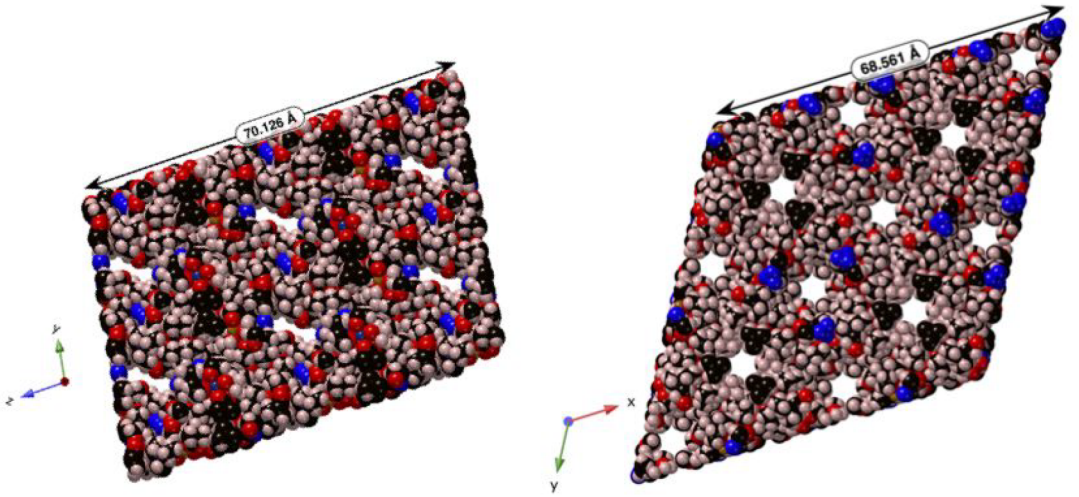

Figure 4. Space filling mode packing of the $P\bar{1}$ and $R\bar{3}$ polymorphs of $[Fe_{18}M_6(piv)_{12}(Htea)_{18}(tea)_6(N_3)_6]$. Specifically, **3a** ($P\bar{1}$ $\{Fe_{18}Gd_6\}$) and **2b** ($R\bar{3}$ $\{Fe_{18}Dy_6\}$) have been drawn in this figure, but their analogues are similar. Note the mainly hydrophobic character of the channels in **2b**.

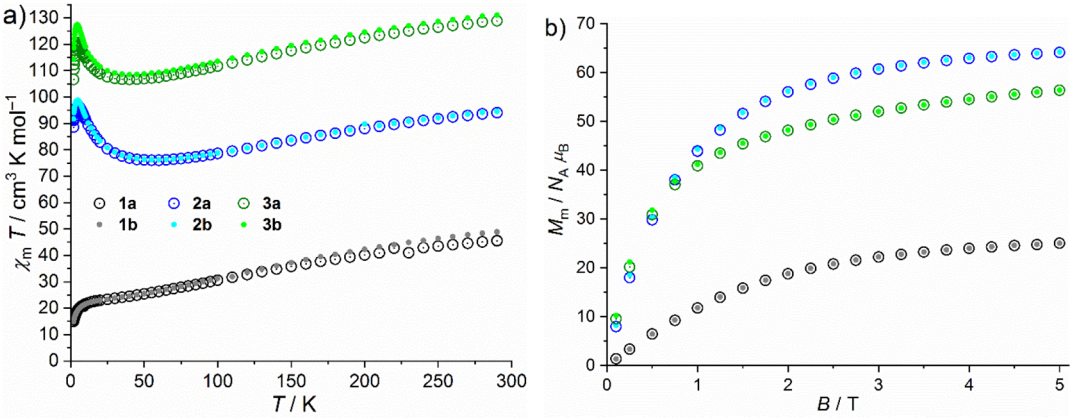

Figure 5. SQUID data of magnetic dc measurements of **1a**−**3b**: (a) $\chi_m T$ vs temperature T at 0.1 T; (b) molar magnetization M_m vs magnetic field B at 2.0 K (symbol and color codes: see a).

Fe(III) centers form six linear Fe_3 trimers that are separated by the Y(III) centers. Due to the high symmetry of the wheel-like compounds, the trimers are considered to be similar. We, thus, normalize the data to such a linear Fe_3 unit (see Figure S10). In the next step, we analyze them in terms of an effective isotropic spin Hamiltonian ($H = -2J_{Fe3}(S_1 \cdot S_2 + S_2 \cdot S_3) + \mu_B g_{eff} \sum_i S_i B$, $g_{eff} = 2.0$) for the intratrimeric exchange interactions and a molecular-field approach for the potential interactions between

https://doi.org/10.1021/acs.cgd.2c00620
Cryst. Growth Des. 2022, 22, 5526−5534

neighboring Fe_3 trimers. The least-squares fits employing the spin-only option of the computational framework CONDON[41] yields the data represented as solid lines in Figure S10. The corresponding fit parameters are $J_{Fe3} = -13.1 \pm 0.4$ cm^{-1}, $\lambda_{mf} = -0.366 \pm 0.112$ mol cm^{-3} ($zJ_{mf} = -0.19 \pm 0.06$ cm^{-1}), and SQ = 3.3% (relative root mean squared error) for **1a** and $J_{Fe3} = -11.6 \pm 0.4$ cm^{-1}, $\lambda_{mf} = -0.368 \pm 0.095$ mol cm^{-3} ($zJ_{mf} = -0.19 \pm 0.05$ cm^{-1}), and SQ = 3.0% for **1b**. The parameter sets of both compounds are rather similar, as expected from structural data. They are also in agreement with the fit parameters found for comparable wheel-like compounds in a previous study.[22] In addition, they show medium antiferromagnetic exchange interactions between the three Fe(III) centers of the trimeric unit and weak intermolecular antiferromagnetic exchange interactions. Finally, the ground states of the Fe_3 trimers in **1a** and **1b** are characterized by a total effective spin of $S_{Fe3} = 5/2$.

The data of the analog compounds **2a**−**3b** are also shown in Figure 5. The diamagnetic Y(III) centers are substituted by paramagnetic lanthanoid centers, in **2a** and **2b** by Gd(III) centers and in **3a** and **3b** by Dy(III) centers. At 290 K, the corresponding $\chi_m T$ values are 94.04 (**2a**) and 94.51 cm^3 K mol^{-1} (**2b**) as well as 128.84 (**3a**) and 131.03 cm^3 K mol^{-1} (**3b**). All of these values are well below the ranges 118.8−128.0 cm^3 K mol^{-1} (**2a**, **2b**) and 151.2−165.3 cm^3 K mol^{-1} (**3a**, **3b**) expected[40] for 18 noninteracting Fe(III) centers and six Gd(III) or six Dy(III) centers, respectively. Taking into account the antiferromagnetic exchange interactions in the trimeric Fe_3 units by subtracting the values of **1a** and **1b**, we obtain the values 48.54 (**2a**), 45.67 (**2b**), 83.34 (**3a**), and 82.19 cm^3 K mol^{-1} (**3b**). Comparison to the expected ranges of the six respective noninteracting lanthanoid centers reveals that the values are close to or within these ranges. Upon decreasing temperatures, the $\chi_m T$ values continuously decrease comparably to the values observed for **1a** and **1b**. However, at 55 K, minima are observed for the Gd(III) analogs and at 40 K for the Dy(III) analogs. Upon further cooling, $\chi_m T$ sharply increases, reaching maxima at about 5 K and subsequently drops off to 88.59 (**2a**), 91.71 (**2b**), 106.64 (**3a**), and 114.23 cm^3 K mol^{-1} (**3b**) at 2.0 K. The molar magnetizations at this temperature (see Figure 5b) distinctly increase up to magnetic fields of 1.5 T and subsequently slightly increase to 64.1 (**2a**), 64.2 (**2b**), and 56.4 $N_A \mu_B$ (**3a**, **3b**), respectively, at 5.0 T, indicating saturation steps.

The observation of the minima and subsequent maxima in the $\chi_m T$ vs T curves reveal the presence of ferromagnetic exchange interactions besides the predominant antiferromagnetic interactions. Taking into account the data analysis of **1a** and **1b**, the ferromagnetic interactions are most likely between the Fe(III) and Ln(III) centers and the antiferromagnetic interactions between Fe(III) centers. The occurrence of the minima at lower temperatures in the case of the Dy(III) analogs is due to the additional contributions originating from the thermal depopulation of the sufficiently split energy states of the Dy(III) centers. For the Gd(III) centers, such effects could be observable at the lowest temperatures and to a much lesser degree, but the data of **2a** and **2b** are dominated in the corresponding temperature range by the ferromagnetic exchange interactions. The values of the molar magnetizations M_m at 2.0 K and 5.0 T are close to the sum of the contributions of the antiferromagnetically coupled Fe_3 trimers (25.0 $N_A \mu_B$ per compound) and the expected contributions of six noninteracting Ln(III) centers, i.e, a saturation value of 7.0 $N_A \mu_B$ per Gd(III) and about half of the saturation value of 10 $N_A \mu_B$ per Dy(III) center. The expectation of about full and half saturation values is due to the data being collected from powder samples of magnetically (almost) isotropic Gd(III) and anisotropic Dy(III) centers, i.e., from randomly oriented crystallites (and Fe(III) centers being isotropic). Note that although Gd(III) centers are virtually isotropic spin-7/2 centers (with $g_{eff} = 1.993$[42]), a system of 18 Fe(III) and six Gd(III) is too large to fit with our approach to shed some insight on the magnitude of the ferromagnetic interactions.

We also analyzed all compounds regarding potential slow relaxation phenomena. Within the limits of the experimental setup, we did not detect relevant out-of-phase signals for compounds **1a**−**2b**. For **3a** and **3b**, we could detect minor signals below 2.8 K, which could, however, not be enhanced by the application of a magnetic bias field (see Figures S11 and S12). Therefore, the data are not suitable for further analysis.

CONCLUSION

The present study represents part of our continuous efforts for preparation of new examples of high-nuclearity 3d/rare earth macrocycles. A series of tetraicosanuclear $\{Fe_{18}M_6\}$ (M = Y, Gd, Dy) pivalate-based wheels were designed as alternatives to the previously reported $\{Fe_{18}M_6\}$ isobutyrate-based wheels (M = Y, Dy, Gd, Tb, Ho, Sm, and Eu). This synthetic approach indicates the main principles for the formation of $\{Fe_{18}M_6\}$-type wheels, such as (*i*) the prerequisite of using μ_3-oxo trinuclear carboxylate clusters as a sole Fe(III) source and (*ii*) ultrasonication facilitating the access to $\{Fe_{18}M_6\}$ wheels. Further research will focus on the introduction of remaining Ln(III) ions into $\{Fe_{18}M_6\}$ pivalate-based wheels as well as the design of corresponding wheel-shaped systems with other carboxylic acids. Additionally, the presence of either MeOH or EtOH in the synthetic process appears to favor the formation of two different polymorphs with triclinic ($P\bar{1}$ for **1a**−**3a** when MeOH is employed) and trigonal ($R\bar{3}$ for **1b**−**3b** when EtOH is employed) symmetries. We plan to follow up on these studies utilizing other solvent media. The investigated dc and ac magnetic susceptibility data show that coupling interactions within the $\{Fe_{18}M_6\}$ pivalate wheel compounds are dominated by antiferromagnetic exchange within Fe_3 units for all compounds and antiferromagnetic (**1a**/**1b**) or ferromagnetic (**2a**/**2b** and **3a**/**3b**) exchange interactions between the Fe(III) and Gd(III) or Dy(III) centers.

ASSOCIATED CONTENT

Supporting Information

The Supporting Information is available free of charge at https://pubs.acs.org/doi/10.1021/acs.cgd.2c00620.

Experimental isotope patterns, table of observed MS fragments, TGA/DSC curves, CSD bond distance analysis, ellipsoid plots of the asymmetric units of **2a** and **3b**, additional magnetic ac measurements plots, IR spectra, crystallographic data, structure refinement parameters, additional crystallographic plots, table of selected bond distances, and bond valence values (BSV) calculations for the Fe atoms in **1**−**3** (PDF)

Accession Codes

CCDC 2169642−2169647 contain the supplementary crystallographic data for this paper. These data can be obtained free of charge via www.ccdc.cam.ac.uk/data_request/cif, or by emailing data_request@ccdc.cam.ac.uk, or by contacting The Cambridge Crystallographic Data Centre, 12 Union Road, Cambridge CB2 1EZ, UK; fax: + 44 1223 336033.

https://doi.org/10.1021/acs.cgd.2c00620
Cryst. Growth Des. 2022, 22, 5526−5534

AUTHOR INFORMATION

Corresponding Authors

Lars Öhrström − *Chemistry and Biochemistry, Department of Chemistry and Chemical Engineering, Chalmers University of Technology, SE-41296 Gothenburg, Sweden;* orcid.org/0000-0002-6420-2141; Email: ohrstrom@chalmers.se

Svetlana G. Baca − *Institute of Applied Physics, MD-2028 Chisinau, Republic of Moldova;* orcid.org/0000-0002-2121-2091; Email: sbaca_md@yahoo.com

Authors

Daniel Podgornii − *Institute of Applied Physics, MD-2028 Chisinau, Republic of Moldova*

Francoise M. Amombo Noa − *Chemistry and Biochemistry, Department of Chemistry and Chemical Engineering, Chalmers University of Technology, SE-41296 Gothenburg, Sweden;* orcid.org/0000-0001-8361-3432

Jan van Leusen − *Institute of Inorganic Chemistry, RWTH Aachen University, 52074 Aachen, Germany;* orcid.org/0000-0003-3688-631X

Christine J. McKenzie − *Department of Physics, Chemistry and Pharmacy, University of Southern Denmark, 5230 Odense M, Denmark;* orcid.org/0000-0001-5587-0626

Paul Kögerler − *Institute of Inorganic Chemistry, RWTH Aachen University, 52074 Aachen, Germany;* orcid.org/0000-0001-7831-3953

Complete contact information is available at: https://pubs.acs.org/10.1021/acs.cgd.2c00620

Notes

The authors declare no competing financial interest.

ACKNOWLEDGMENTS

This work in part was supported by State Programs of the National Agency for Research and Development of R. Moldova 20.80009.5007.15 (project "Implementation of crystal engineering approach and X-ray crystallography for design and creation of hybrid organic/inorganic materials with advanced physical and biologically active functions"). S.G.B. is grateful to the Alexander von Humboldt Foundation for a Georg Forster Research Award and the Swedish Institute for financial support under the Visby Program. C.J.M. is grateful to the Carlsberg Foundation for funding (grant CF15-0675) for the single crystal X-ray diffractometer. Authors thank Jürg Hauser for collecting X-ray data sets for **3a**.

REFERENCES

(1) Cook, T. R.; Stang, P. J. Recent Developments in the Preparation and Chemistry of Metallacycles and Metallacages via Coordination. *Chem. Rev.* **2015**, *115*, 7001−7045.

(2) McInnes, E. J. L.; Timco, G. A.; Whitehead, G. F. S.; Winpenny, R. E. P. Heterometallic Rings: Their Physics and Use as Supramolecular Building Blocks. *Angew. Chem., Int. Ed.* **2015**, *54*, 14244−14269.

(3) Boulon, M.-E.; Fernandez, A.; Moreno Pineda, E.; Chilton, N. F.; Timco, G.; Fielding, A. J.; Winpenny, R. E. P. Measuring Spin···Spin Interactions between Heterospins in a Hybrid [2]Rotaxane. *Angew. Chem., Int. Ed.* **2017**, *56*, 3876−3879.

(4) Tasiopoulos, A. J.; Vinslava, A.; Wernsdorfer, W.; Abboud, K. A.; Christou, G. Giant Single-Molecule Magnets: A $\{Mn_{84}\}$ Torus and Its Supramolecular Nanotubes. *Angew. Chem., Int. Ed.* **2004**, *43*, 2117−2121.

(5) Zhang, Z. M.; Li, Y. G.; Yao, S.; Wang, E. B.; Wang, Y. H.; Clérac, R. Enantiomerically pure chiral $\{Fe_{28}\}$ wheels. *Angew. Chem., Int. Ed.* **2009**, *48*, 1581−1584.

(6) Bi, Y.; Xu, G.; Liao, W.; Du, S.; Wang, X.; Deng, R.; Zhang, H.; Gao, S. Making a $[Co_{24}]$ metallamacrocycle from the shuttlecock-like tetranuclear cobalt-calixarene building blocks. *Chem. Commun.* **2010**, *46*, 6362−6364.

(7) Cadiou, C.; Murrie, M.; Paulsen, C.; Villar, V.; Wernsdorfer, W.; Winpenny, R. E. P. Studies of a nickel-based single molecule magnet: resonant quantum tunnelling in an S = 12 molecule. *Chem. Commun.* **2001**, 2666−2667.

(8) Ferrando-Soria, J.; Moreno Pineda, E.; Chiesa, A.; Fernandez, A.; Magee, S. A.; Carretta, S.; Santini, P.; Vitorica-Yrezabal, I. J.; Tuna, F.; Timco, G. A.; McInnes, E. J. L.; Winpenny, R. E. P. A modular design of molecular qubits to implement universal quantum gates. *Nat. Commun.* **2016**, *7*, 11377.

(9) Stamatatos, T. C.; Mukherjee, S.; Abboud, K. A.; Christou, G. The largest single-strand molecular wheel: Ga_{20} from a targeted, diolate-induced size modification of the Ga_{10} 'gallic wheel'. *Chem. Commun.* **2009**, 62−64.

(10) Shi, D.; Yang, X.; Chen, H.; Ma, Y.; Schipper, D.; Jones, R. A. Self-assembly of luminescent 42-metal lanthanide nanowheels with sensing properties towards metal ions and nitro explosives. *J. Mater. Chem. C* **2019**, *7*, 13425−13431.

(11) Zheng, X.-Y.; Jiang, Y.-H.; Zhuang, G.-L.; Liu, D.-P.; Liao, H.-G.; Kong, X.-J.; Long, L.-S.; Zheng, L.-S. A Gigantic Molecular Wheel of $\{Gd_{140}\}$: A New Member of the Molecular Wheel Family. *J. Am. Chem. Soc.* **2017**, *139*, 18178−18181.

(12) Biswas, S.; Das, S.; Acharya, J.; Kumar, V.; van Leusen, J.; Kögerler, P.; Herrera, J. M.; Colacio, E.; Chandrasekhar, V. Homometallic Dy^{III} Complexes of Varying Nuclearity from 2 to 21: Synthesis, Structure, and Magnetism. *Chem.—Eur. J.* **2017**, *23*, 5154−5170.

(13) Wang, K.; Chen, Z.-L.; Zou, H.-H.; Hu, K.; Li, H. Y.; Zhang, Z.; Sun, W.-Y.; Liang, F.-P. A single-stranded $\{Gd_{18}\}$ nanowheel with a symmetric polydentate diacylhydrazone ligand. *Chem. Commun.* **2016**, *52*, 8297−8300.

(14) Zou, L.-F.; Zhao, L.; Guo, Y.-N.; Yu, G.-M.; Guo, Y.; Tang, J.; Li, Y.-H. A dodecanuclear heterometallic dysprosium−cobalt wheel exhibiting single-molecule magnet behavior. *Chem. Commun.* **2011**, *47*, 8659−8661.

(15) Ojea, M. J. H.; Lorusso, G.; Craig, G. A.; Wilson, C.; Evangelisti, M.; Murrie, M. A topologically unique alternating $\{Co^{III}_3Gd^{III}_3\}$ magnetocaloric ring. *Chem. Commun.* **2017**, *53*, 4799−4802.

(16) Zhang, L.; Zhao, L.; Zhang, P.; Wang, Ch.; Yuan, S.-W.; Tang, J. Nanoscale $\{Ln^{III}_{24}Zn^{II}_6\}$ Triangular Metalloring with Magnetic Refrigerant, Slow Magnetic Relaxation, and Fluorescent Properties. *Inorg. Chem.* **2015**, *54*, 11535−11541.

(17) Li, M.; Lan, Y.; Ako, A. M.; Wernsdorfer, W.; Anson, Ch. E.; Buth, G.; Powell, A. K.; Wang, Zh.; Gao, S. A Family of 3d-4f Octa-Nuclear $[Mn^{III}_4Ln^{III}_4]$ Wheels (Ln = Sm, Gd, Tb, Dy, Ho, Er, and Y): Synthesis, Structure, and Magnetism. *Inorg. Chem.* **2010**, *49*, 11587−11594.

(18) Zou, L.-F.; Zhao, L.; Guo, Y.-N.; Yu, G.-M.; Guo, Y.; Tang, J.; Li, Y.-H. A dodecanuclear heterometallic dysprosium-cobalt wheel exhibiting single-molecule magnet behavior. *Chem. Commun.* **2011**, *47*, 8659−8661.

(19) Baniodeh, A.; Hewitt, I. J.; Mereacre, V.; Lan, Y.; Novitchi, G.; Anson, C. E.; Powell, A. K. Heterometallic 20-membered $\{Fe_{16}Ln_4\}$ (Ln = Sm, Eu, Gd, Tb, Dy, Ho) metallo-ring aggregates. *Dalton Trans.* **2011**, *40*, 4080−4086.

(20) Zhang, Z.-M.; Pan, L.-Y.; Lin, W.-Q.; Leng, J.-D.; Guo, F.-Sh.; Chen, Y.-C.; Liu, J.-L.; Tong, M.-L. Wheel-shaped nanoscale 3d−4f $\{Co^{II}_{16}Ln^{III}_{24}\}$ clusters (Ln = Dy and Gd). *Chem. Commun.* **2013**, *49*, 8081−8083.

(21) Leng, J.-D.; Liu, J.-L.; Tong, M.-L. Unique nanoscale $\{Cu^{II}_{36}Ln^{III}_{24}\}$ (Ln = Dy and Gd) metallo-rings. *Chem. Commun.* **2012**, *48*, 5286−5288.

(22) Botezat, O.; van Leusen, J.; Kravtsov, V. Ch.; Kögerler, P.; Baca, S. G. Ultralarge 3d/4f Coordination Wheels: From Carboxylate/Amino Alcohol-Supported $\{Fe_4Ln_2\}$ to $\{Fe_{18}Ln_6\}$ Rings. *Inorg. Chem.* **2017**, *56*, 1814−1822.

(23) Gerbeleu, N. V.; Batsanov, A. S.; Timko, G. A.; Struchkov, Yu. T.; Indrichan, K. M.; Popovich, G. A. Synthesis and structure of tri- and hexanuclear μ_3-oxopivalates of iron(III). *Dokl. Akad. Nauk SSSR* **1987**, *293*, 364−367.
(24) Batsanov, A. S.; Struchkov, Yu. T.; Timko, G. A. Crystal structure of hexanuclear iron(III) pivalate, $Fe_3(\mu_3\text{-}O)_2(\mu\text{-}OH)_2(\mu\text{-}Me_3CCO_2)_{12}$. *Koord. Khim. (in Russian)* **1988**, *14*, 266−270.
(25) *SAINT-Plus*, version 8.34; Bruker AXS Inc.: Madison, WI, 2004.
(26) Sheldrick, G. M. SADABS, software for empirical absorption correction, version 2.05; University of Göttingen: Germany, 2004.
(27) Krause, L.; Herbst-Irmer, R.; Sheldrick, G. M.; Stalke, D. Comparison of Silver and Molybdenum microfocus X-ray sources for single-crystal structure determination. *J. Appl. Crystallogr.* **2015**, *48*, 3−10.
(28) *Crysalis CCD*; Oxford Diffraction Ltd.: Abingdon, Oxfordshire, UK, 2005.
(29) *Crysalis RED*; Oxford Diffraction Ltd.: Abingdon, Oxfordshire, UK, 2005.
(30) Sheldrick, G. Crystal structure refinement with SHELXL. *Acta Crystallogr.* **2015**, *C71*, 3−8.
(31) Barbour, L. X-Seed 4: updates to a program for small-molecule supramolecular crystallography. *J. Appl. Crystallogr.* **2020**, *53*, 1141−1146.
(32) Images generated using: *CrystalMaker: a crystal and molecular structures program for Mac and Windows*; CrystalMaker Software Ltd: Oxford, UK, 2019.
(33) Spek, A. L. PLATON SQUEEZE: a tool for the calculation of disordered solvent contribution to the calculated structure factors. *Acta Crystallogr. C Struct Chem.* **2015**, *71*, 9−18.
(34) Botezat, O.; van Leusen, J.; Kögerler, P.; Baca, S. G. Tuning the condensation degree of $\{Fe^{III}_n\}$ oxo clusters via ligand metathesis, temperature and solvents. *Inorg. Chem.* **2018**, *57*, 7904−7913.
(35) Baca, S. G.; Speldrich, M.; van Leusen, J.; Ellern, A.; Kögerler, P. Undecametallic and hexadecametallic ferric oxo−hydroxo/ethoxo pivalate clusters. *Dalton Trans.* **2015**, *44*, 7777−7780.
(36) Baca, S. G.; Speldrich, M.; Ellern, A.; Kögerler, P. $\{Fe_6O_2\}$-Based assembly of a tetradecanuclear iron nanocluster. *Materials* **2011**, *4*, 300−310.
(37) Bang, J. H.; Suslick, K. S. Applications of Ultrasound to the Synthesis of Nanostructured Materials. *Adv. Mater.* **2010**, *22*, 1039−1059.
(38) Botezat, O.; van Leusen, J.; Kögerler, P.; Baca, S. G. Ultrasound-Assisted Formation of $\{Fe_6Ln/Y_4\}$ Wheel-Shaped Clusters and Condensed $\{Fe_4Ln/Y_2\}$ Aggregates. *Eur. J. Inorg. Chem.* **2019**, *2019*, 2236−2244.
(39) Darii, M.; Kravtsov, V.Ch; Krämer, K.; Hauser, J.; Decurtins, S.; Liu, S.-X.; Affronte, M.; Baca, S. G. Aggregation of a Giant Bean-like $\{Mn_{26}Dy_6\}$ Heterometallic Oxo-Hydroxo-Carboxylate Nanosized Cluster from a Hexanuclear $\{Mn_6\}$ Precursor. *Cryst. Growth Des.* **2020**, *20*, 33−38.
(40) Lueken, H. *Magnetochemie*; Teubner Verlag: Stuttgart, 1999.
(41) Speldrich, M.; van Leusen, J.; Kögerler, P. CONDON 3.0: An Updated Software Package for Magnetochemical Analysis - All the Way to Polynuclear Actinide Complexes. *J. Comput. Chem.* **2018**, *39*, 2133−2145.
(42) Sytsma, J.; Murdoch, K. M.; Edelstein, N. M.; Boatner, L. A.; Abraham, M. M. Spectroscopic Studies and crystal-field analysis of Cm^{3+} and Gd^{3+} in $LuPO_4$. *Phys. Rev. B* **1995**, *52*, 12668−12676.

https://doi.org/10.1021/acs.cgd.2c00620
Cryst. Growth Des. 2022, 22, 5526−5534